

Time evolution of the intensity and size of tropical cyclones

Kate D. Musgrave,¹ Richard K. Taft,² Jonathan L. Vigh,³ Brian D. McNoldy,⁴ and Wayne H. Schubert²

Received 31 October 2011; revised 12 April 2012; accepted 9 May 2012; published 2 August 2012.

[1] The purpose of this paper is to analyze the life cycle of tropical cyclones in terms of a K - V_{\max} diagram. Such a diagram summarizes the time evolution of the integrated kinetic energy K and the maximum tangential wind V_{\max} , which respectively measure vortex size and intensity. A typical life cycle consists of an incipient stage in which K and V_{\max} slowly increase until $V_{\max} \approx 25 \text{ m s}^{-1}$, a deepening stage in which K and V_{\max} increase more rapidly until $V_{\max} \approx 60 \text{ m s}^{-1}$, and finally a mature stage in which K continues to grow at approximately the same rate while V_{\max} remains fixed or even decreases. This typical life cycle can be diagnostically analyzed using a theoretical argument that is based on the balanced vortex model and, in particular, on the associated geopotential tendency equation. This is a second order partial differential equation containing the diabatic forcing and, under idealized conditions, two spatially varying coefficients: the static stability and the inertial stability, whose ratio determines the local Rossby length ℓ . Thus, the balanced azimuthal wind and temperature tendencies in a tropical vortex depend not only on the diabatic forcing, but also on the spatial distribution of ℓ . Under the simplifying assumption that the diabatic heating and the associated response are confined to the first internal vertical mode, the geopotential tendency equation reduces to a radial structure equation, which can be solved numerically. These solutions illustrate how the vortex response to diabatic heating depends on whether this heating lies in the large Rossby length region outside the radius of maximum wind or in the small Rossby length region inside the radius of maximum wind. Tangential wind tendencies are found to be hypersensitive to the location of the diabatic heating relative to the small Rossby length region in the vortex core.

Citation: Musgrave, K. D., R. K. Taft, J. L. Vigh, B. D. McNoldy, and W. H. Schubert (2012), Time evolution of the intensity and size of tropical cyclones, *J. Adv. Model. Earth Syst.*, 4, M08001, doi:10.1029/2011MS000104.

1. Introduction

[2] The first success in modeling the life cycle of tropical cyclones was obtained by Ooyama [1969], using a model of maximum simplification: axisymmetric, hydrostatic, gradient balanced, with only three layers and with moisture predicted only in the lowest layer. Despite its simplicity, the results of numerical integrations showed that the model was capable of simulating typical tropical cyclone life cycles with a remarkable degree of reality. The results of a typical case are summarized in Figure 1, which shows the time evolution of the maximum tangential wind, the radius of maximum

tangential wind, the radius of hurricane force wind (64 kt), the radius of gale force wind (34 kt), the radius of maximum upward Ekman pumping at the top of the boundary layer, and the minimum surface pressure. The storm intensifies from 10 m s^{-1} to 58 m s^{-1} in 134 h, after which the maximum wind slowly decreases while the size of the storm continues to grow, as indicated by the outward movement of the radius of gale force winds and the radius of hurricane force winds. The growth in storm size is also clearly illustrated in Figure 2, which depicts the time evolution of the integrated kinetic energy inside radii of 100, 200, 500, and 1000 km. Note that, after the peak wind speed at 134 h, there is continued rapid growth in the total kinetic energy inside 1000 km. After 100 h, less than half of the integrated kinetic energy comes from the region inside 200 km.

[3] Another way to summarize this idealized case is with a K - V_{\max} diagram, i.e., a diagram in which the ordinate is the integrated kinetic energy inside a radius of 1000 km and the abscissa is the maximum tangential wind. The time evolution of Ooyama's case is shown by the multi-colored curve in the K - V_{\max} diagram shown in Figure 3. The life cycle has been broken into three stages:

¹Cooperative Institute for Research in the Atmosphere, Colorado State University, Fort Collins, Colorado, USA.

²Department of Atmospheric Science, Colorado State University, Fort Collins, Colorado, USA.

³Research Applications Laboratory, National Center for Atmospheric Research, Boulder, Colorado, USA.

⁴Rosenstiel School of Marine and Atmospheric Science, University of Miami, Miami, Florida, USA.

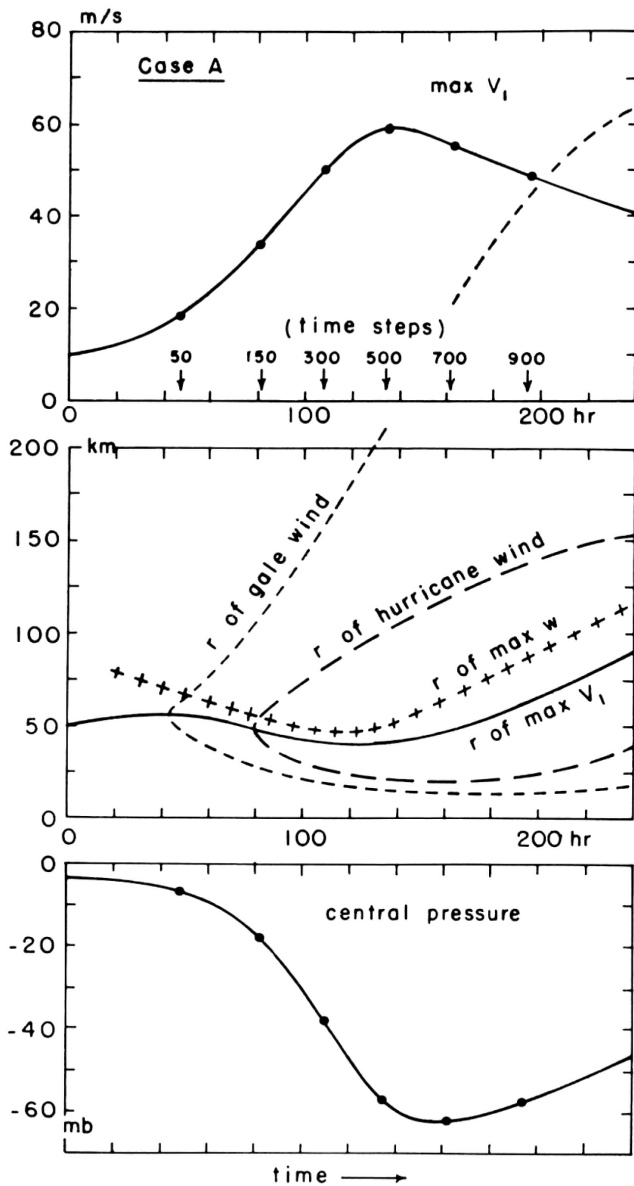


Figure 1. Time evolution of (top) the maximum tangential wind, (middle) the radii of maximum wind, hurricane force wind, gale force wind, and maximum Ekman pumping, and (bottom) the central surface pressure. From *Ooyama* [1969].

incipient (0–60 h), deepening (60–134 h), and mature (134–216 h). As can be seen from Figure 3, there is an obvious inadequacy to a single scale based on V_{\max} only. For example, the simulated storm has $V_{\max} \approx 44 \text{ m s}^{-1}$ (Category 2 on the Saffir-Simpson scale) at both $t \approx 96 \text{ h}$ and $t \approx 216 \text{ h}$, but these two times have kinetic energies differing by approximately a factor of six. At $t \approx 96 \text{ h}$ the simulated storm is small and in the deepening stage, while at $t \approx 216 \text{ h}$ it is large and in the mature stage. This inadequacy of the Saffir-Simpson scale has led to proposals by *Powell and Reinhold* [2007] and by *Maclay et al.* [2008] for a two-parameter storm classification based on maximum wind and integrated kinetic energy.

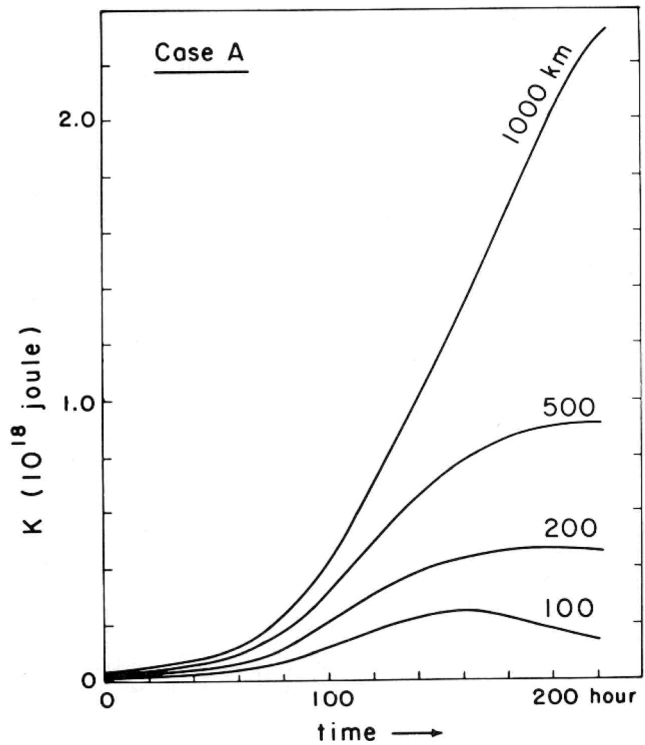


Figure 2. Time evolution of the total kinetic energy for regions within radii of 100, 200, 500, and 1000 km. From *Ooyama* [1969].

[4] Although the multi-colored curve in Figure 3 shows a typical tropical cyclone life cycle in the K - V_{\max} plane, considerable variability from this curve can occur in real and model cyclones. For example, *Zehr and Knaff* [2007] have shown observationally that hurricane size, as given by the average radius of gale-force winds (see the approximate ordinate scale on the right side of Figure 3), is approximately 251 km when the storm is at maximum intensity. Although this agrees fairly well with the multi-colored curve in Figure 3, *Zehr and Knaff* point out the extremely large variability in this value, which ranges from 93 to 427 km in their data set. Further variations from the multi-colored curve in Figure 3 occur in annular hurricanes [*Knaff et al.*, 2003a, 2008], which tend to maintain high values of V_{\max} while K increases.

[5] Another type of variability occurs with small intense hurricanes. For example, Hurricane Inez (1966), described in detail by *Hawkins and Imbembo* [1976], was an intense hurricane whose radii of gale force and hurricane force winds near the time of peak intensity were approximately half those of the typical case shown in Figures 1–3. Even more extreme cases of small intense typhoons occur in the western Pacific [e.g., see *Arakawa*, 1952; *Brand*, 1972; *Merrill*, 1984; *Weatherford and Gray*, 1988a, 1988b; and *Harr et al.*, 1996]. A classic example of a small intense storm is Cyclone Tracy, which had gale force winds extending only 50 km from its center when it struck Darwin, Australia in December 1974. Such behavior is indicated in the lower part of Figure 3 with the label “Strong Dwarfs.” At the other

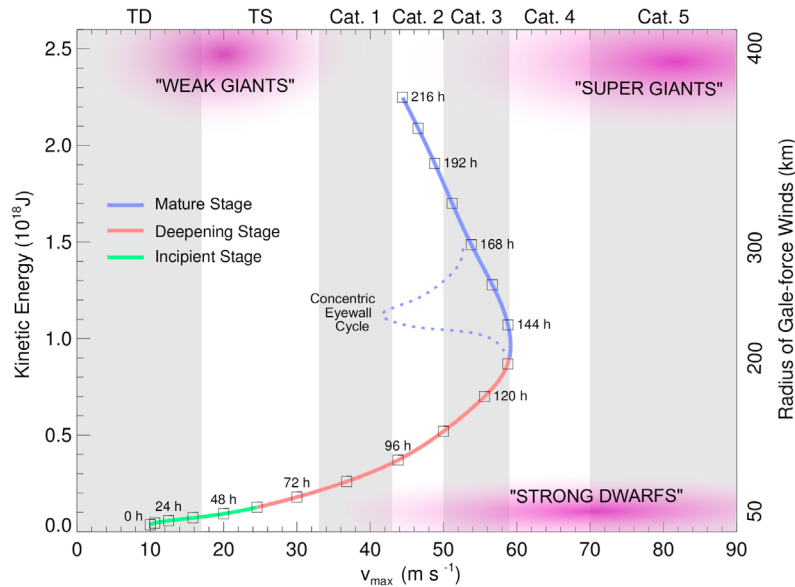


Figure 3. The multi-colored curve shows the K - V_{\max} time evolution of the model vortex shown in Figures 1 and 2. The incipient, deepening, and mature stages are indicated respectively by green, red, and blue. Time marks are every 12 h. Labels across the top of the figure stand for tropical depression (TD), tropical storm (TS), and the five Saffir-Simpson categories. Excursions off this “main sequence” can be caused by potential vorticity mixing and concentric eyewall cycles (the latter of which is shown schematically as a sudden decrease in V_{\max} as the inner eyewall dies). Three other types of time evolution occur in small, intense storms labeled here as “Strong Dwarfs,” in large, mature storms labeled here as “Super Giants,” and in large tropical depressions or tropical storms that never reach hurricane intensity, labeled here as “Weak Giants.” For rough quantitative interpretation, the ordinate is also labeled (on the right) in terms of the radius of gale-force winds.

extreme are the western Pacific’s mature supertyphoons, which, as indicated in the upper-right part of Figure 3, can simultaneously have large K and large V_{\max} . The prototype of these storms is Super Typhoon Tip (1979), as described by *Dunnavan and Diercks* [1980]. At its most intense stage, Tip had winds of 85 m s^{-1} and a radius of hurricane force winds more than double that shown in Figure 1, and an 1100 km radius of gale force winds, so its K would be well off the upper edge of Figure 3. We have indicated such storms in the upper-right part of Figure 3 with the label “Super Giants.” Finally, on the left side of Figure 3 we have indicated a class of storms called “Weak Giants,” which are tropical depressions or tropical storms that, although never reaching hurricane intensity, can become quite large and produce copious rainfall. The nomenclature used in Figure 3 is modeled after the Hertzsprung-Russell diagram, which is a scatterplot showing the relationship of stars in terms of their absolute magnitude and effective temperature [*Rosenberg*, 1910]. On the H-R diagram, one finds a main sequence region (our multi-colored curve), as well as hot white dwarfs (our strong dwarfs), cool supergiants (our weak giants), and hot supergiants (our super giants) that highlight excursions from the main sequence.

[6] There are two important phenomena that can cause variability from the typical “main sequence” curve in Figure 3. The first is potential vorticity mixing [*Schubert et al.*, 1999; *Kossin and Eastin*, 2001; *Montgomery et al.*, 2002; *Hendricks et al.*, 2009; *Hendricks and Schubert*, 2010]. This process, which is

often associated with polygonal eyewalls, tends to reduce V_{\max} but leave K relatively unchanged. A second source of variability of curves in the K - V_{\max} plane is the concentric eyewall cycle, a process in which intensification is interrupted by the formation of an outer eyewall, the decay of the inner eyewall, and finally the contraction of the outer eyewall [*Willoughby et al.*, 1982; *Houze et al.*, 2007; *Rozoff et al.*, 2008; *Terwey and Montgomery*, 2008; *Didlake and Houze*, 2011]. The K - V_{\max} signature of an eyewall cycle for an intense tropical cyclone is shown schematically by the dotted curve near the center of Figure 3, which resembles a hairpin turn on the road to maturity.

[7] An interesting feature in Figure 1 (middle) is that the radius of maximum Ekman pumping (and hence the region of strong diabatic heating) always lies outside the radius of maximum tangential wind, but during the period of rapid increase in V_{\max} , the region of diabatic heating moves inward toward the high inertial stability region that lies just inside the radius of maximum wind. In contrast, during the later mature period of increasing K and slowly decreasing V_{\max} (i.e., after 132 h), the region of diabatic heating shifts outward, away from the region of largest inertial stability. This general behavior is consistent with the observational results of *Corbosiero et al.* [2005], who performed a detailed analysis of Hurricane Elena (1985) during a 28-h period when it was well observed by both ground-based radar and aircraft. Their results indicate that Elena’s period of most rapid intensification occurred when intense convection

was located close to the region of high inertial stability. Sections 3 and 4 provide further discussion of this important aspect of tropical cyclone dynamics.

[8] The results shown in Figures 1–3 were produced by a three layer model that uses the gradient balance approximation in all three layers. The use of gradient balance in the calculation of the boundary layer inflow is probably the weakest assumption in the model. When the boundary layer radial inflow is strong, the neglect of the radial advection term $u(\partial u/\partial r)$ is not justifiable. In a companion study, *Ooyama* [1968] relaxed the assumption of gradient balance in the boundary layer in order to produce a more accurate radial distribution of Ekman pumping. More detailed discussions of the role of the $u(\partial u/\partial r)$ term in hurricane boundary layer dynamics can be found in *Shapiro* [1983], *Smith and Vogl* [2008], *Smith and Montgomery* [2008], *Smith et al.* [2009], *Bui et al.* [2009], *Kepert* [2010a, 2010b], and *G. J. Williams et al.* (Shock-like structures in the tropical cyclone boundary layer, submitted to *Journal of Advances in Modeling Earth Systems*, 2012). Figures 4 and 5 show how the results of Figure 1 are modified when this more accurate boundary layer formulation is incorporated. With the inclusion of the $u(\partial u/\partial r)$ term in the boundary layer radial momentum equation, the peak Ekman pumping lies at $r \approx 16$ km, i.e., on the inside edge of the eyewall rather than at $r \approx 57$ km, on the outside edge of the eyewall (Figure 5b). This places the diabatic heating closer to the region of high inertial stability so that the storm's V_{\max} increases more rapidly (see Figure 4a) and the integrated kinetic energy increases more slowly. These results are consistent with the notion that evolution curves on a K - V_{\max} diagram depend crucially on the spatial proximity of the maximum values of inertial stability and diabatic heating.

[9] The purpose of the present paper is to use a simple diagnostic tool derived from the balanced vortex model to show how the relative radial positioning of high inertial stability and strong diabatic heating determines how a storm evolves in the K - V_{\max} plane. The simple diagnostic tool is developed in section 2, and then applied to a 30 m s^{-1} vortex in section 3 and to vortices of various strengths in section 4. Some concluding remarks about hurricane intensity forecasting are given in section 5.

2. Balanced Vortex Model

[10] We consider inviscid, axisymmetric, quasi-static, gradient-balanced motions of a stratified, compressible atmosphere on an f -plane. As the vertical coordinate we use $z = H \ln(p_0/p)$, where $H = RT_0/g$, with p_0 and T_0 denoting constant reference values of pressure and temperature. The governing equations for the balanced vortex model are

$$\left(f + \frac{v}{r}\right)v = \frac{\partial \phi}{\partial r}, \quad (1)$$

$$\frac{\partial v}{\partial t} + u \left(f + \frac{\partial(rv)}{\partial r}\right) + w \frac{\partial v}{\partial z} = 0, \quad (2)$$

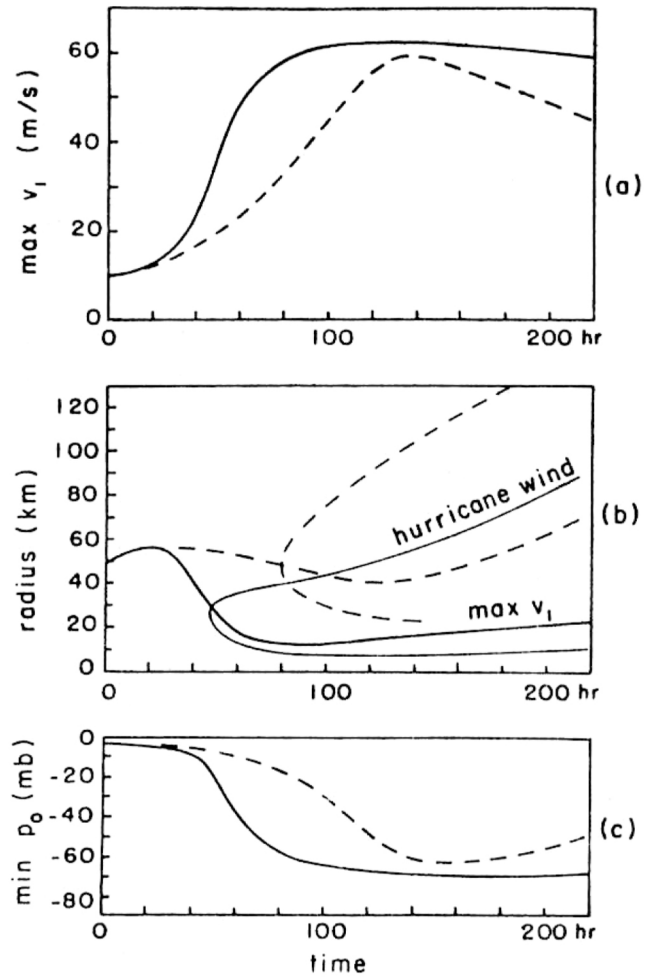


Figure 4. Time evolution of (a) the maximum tangential wind, (b) the radii of maximum wind and hurricane force wind, and (c) the central surface pressure. Dashed lines are for Model I, which assumes gradient balance in all three model layers. Solid lines are for Model II, which includes the $u(\partial u/\partial r)$ term in boundary layer radial momentum equation. Note that the dashed curves are identical to the curves shown in Figure 1. From *Ooyama* [1968].

$$\frac{\partial \phi}{\partial z} = \frac{g}{T_0} T, \quad (3)$$

$$\frac{\partial(rv)}{\partial r} + \frac{\partial w}{\partial z} - \frac{w}{H} = 0, \quad (4)$$

$$\frac{\partial T}{\partial t} + u \frac{\partial T}{\partial r} + w \left(\frac{\partial T}{\partial z} + \frac{RT}{c_p H}\right) = \frac{Q}{c_p}, \quad (5)$$

where u and v are the radial and tangential components of velocity, w is the ‘log-pressure vertical velocity’, ϕ is the geopotential, f is the constant Coriolis parameter,

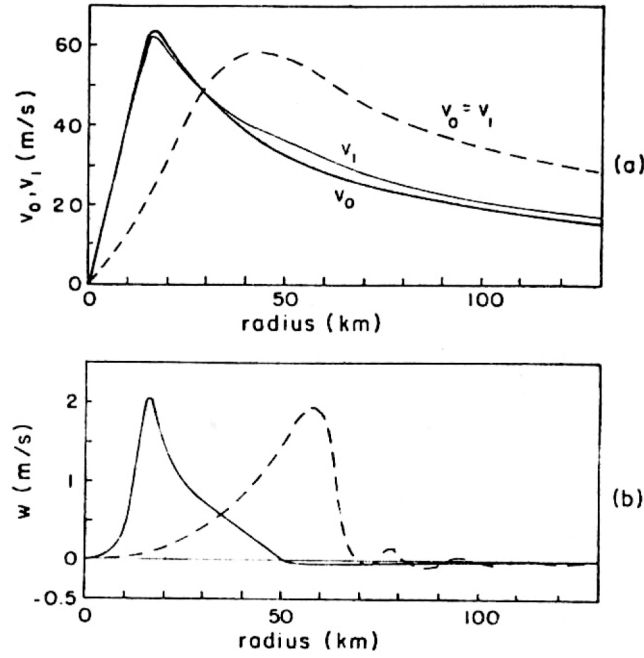


Figure 5. (a) The radial distribution of v_0 , the azimuthal wind in the boundary layer, and v_1 , the azimuthal wind in the lower main layer for Model I (dashed line) and Model II (solid lines). (b) The radial distribution of w , the vertical velocity at the top of the Ekman layer, for Model I (dashed) and Model II (solid). All curves are for $t=146$ hours. From Ooyama [1968].

and Q is the diabatic heating. The total energy principle associated with the governing equations (1)–(5) is

$$\frac{d}{dt} \iint \left(\frac{1}{2} v^2 + c_p T \right) e^{-z/H} r dr dz = \iint Q e^{-z/H} r dr dz. \quad (6)$$

Because of the gradient balance assumption (1), the radial velocity component does not appear in (6).

[11] Equations (1)–(5) constitute a system of five equations in the six unknowns u, v, w, ϕ, T, Q , so obviously an additional “parameterization” relating Q to the other unknowns is required for closure. However, as is apparent from the discussion in section 1, the addition of a parameterization relation for Q would require incorporation of boundary layer dynamics, since the boundary layer radial inflow is crucial in determining the location and strength of eyewall convection. In order to keep the theoretical argument as simple as possible, we attempt to see what conclusions can be drawn about the relationships between the vortex structure, the temperature and tangential wind tendencies, and the diabatic heating, without making use of such a comparatively uncertain parameterization relation for Q .

[12] As a hurricane evolves, the spatial distributions of the static stability, baroclinicity, and inertial stability change. The changes in the inertial stability can be particularly large, with important implications for the spatial

distribution of tendencies of the wind and mass fields. To isolate the important role of changes in the inertial stability, we seek solutions of (1)–(5) under the assumption that the baroclinic terms $w(\partial v/\partial z)$ and $u(\partial T/\partial r)$ can be neglected. Near the vortex core of a hurricane the baroclinic terms do play an important role in producing an outward tilt to the eyewall updraft [Pendergrass and Willoughby, 2009; Schubert and McNoldy, 2010], so the present analysis will not capture this effect. However, an important advantage of the approach followed here is that it leads to insight about the role of vorticity skirts using very simple mathematical methods. Thus, neglecting the baroclinic terms, we now multiply the thermodynamic equation by g/T_0 and the tangential wind equation by $f+(2v/r)$, and then make use of the gradient and hydrostatic relations to obtain

$$\frac{\partial \phi_t}{\partial z} + N^2 w = \frac{g}{c_p T_0} Q, \quad (7)$$

$$\frac{\partial \phi_t}{\partial r} + \hat{f}^2 u = 0, \quad (8)$$

where $\phi_t = \partial \phi / \partial t$ denotes the geopotential tendency, and where the static stability and the inertial stability are given by

$$N^2 = \frac{g}{T_0} \left(\frac{\partial T}{\partial z} + \frac{RT}{c_p H} \right), \quad (9)$$

$$\hat{f}^2 = \left(f + \frac{2v}{r} \right) \left(f + \frac{\partial(rv)}{r \partial r} \right). \quad (10)$$

In the following analysis we shall consider N^2 to be a constant and \hat{f}^2 to be a function of r only.

[13] We can now regard (4), (7), and (8) as a system in u, w, ϕ_t . One way of proceeding from (7) and (8) is to eliminate ϕ_t to obtain an equation for the transverse circulation [e.g., Shapiro and Willoughby, 1982; Schubert and Hack, 1982]. The solution of this transverse circulation equation yields the radial and vertical velocity components, which can then be substituted into the azimuthal wind and thermodynamic equations to obtain the tendencies of v and T . A more direct route to the tendencies is obtained by using the continuity equation to eliminate u and w between (7) and (8), thereby obtaining the tendency equation

$$N^2 \frac{\partial}{\partial r} \left(\frac{r}{\hat{f}^2} \frac{\partial \phi_t}{\partial r} \right) + \left(\frac{\partial}{\partial z} - \frac{1}{H} \right) \frac{\partial \phi_t}{\partial z} = \frac{g}{c_p T_0} \left(\frac{\partial}{\partial z} - \frac{1}{H} \right) Q. \quad (11)$$

Equation (11) is a second order partial differential equation for ϕ_t . To obtain boundary conditions for (11) we assume that Q and w vanish along the top and bottom boundaries, so that (7) yields

$$\frac{\partial \phi_t}{\partial z} = 0 \text{ at } z=0, z_T. \quad (12)$$

Since u vanishes along the axis of symmetry and $ru \rightarrow 0$ as $r \rightarrow \infty$, (8) yields

$$\frac{\partial \phi_t}{\partial r} = 0 \text{ at } r=0, \text{ and } r\phi_t \rightarrow 0 \text{ as } r \rightarrow \infty. \quad (13)$$

Here we consider only vortices with $\hat{f}N > 0$ everywhere, which ensures that (11)–(13) is an elliptic problem.

[14] We now solve (11)–(13) via separation of variables, assuming that $Q(r, z)$ has the vertical structure given below in the top line of (14). It is easily shown that $T_t(r, z)$ and $w(r, z)$ have the same vertical structure and that $\phi_t(r, z)$, $v_t(r, z)$, and $u_t(r, z)$ have the vertical structure given in (15). The two vertical structure functions appearing in (14) and (15) are plotted in Figure 6. The blue curve is the vertical structure function $\exp[z/(2H)]\sin(\pi z/z_T)$, which reaches its maximum at $z=z_m$, where z_m is given by $\pi z_m/z_T = \pi + \tan^{-1}(-2\pi H/z_T)$. For $z_T = 15$ km and $H = RT_0/g = 8.718$ km, the formula for z_m yields $z_m \approx 8.776$ km, which results in a maximum value of 1.596 for the vertical structure function. Then, using the separable forms

$$\begin{pmatrix} Q(r, z) \\ T_t(r, z) \\ w(r, z) \end{pmatrix} = \begin{pmatrix} \hat{Q}(r) \\ \hat{T}_t(r) \\ \hat{w}(r) \end{pmatrix} \exp\left(\frac{z}{2H}\right) \sin\left(\frac{\pi z}{z_T}\right), \quad (14)$$

$$\begin{pmatrix} \phi_t(r, z) \\ v_t(r, z) \\ u_t(r, z) \end{pmatrix} = \begin{pmatrix} \hat{\phi}_t(r) \\ \hat{v}_t(r) \\ \hat{u}_t(r) \end{pmatrix} \exp\left(\frac{z}{2H}\right) \cdot \left[\cos\left(\frac{\pi z}{z_T}\right) - \frac{z_T}{2\pi H} \sin\left(\frac{\pi z}{z_T}\right) \right], \quad (15)$$

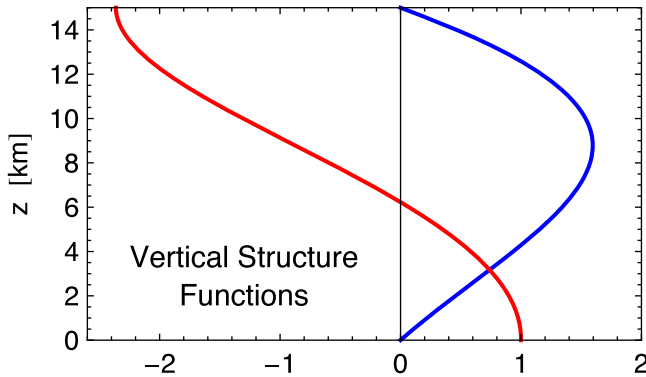


Figure 6. Vertical structure functions appearing in (14) and (15). The blue curve is $\exp[z/(2H)]\sin(\pi z/z_T)$, the vertical structure function for $Q(r, z), T_t(r, z), w(r, z)$. The red curve is $\exp[z/(2H)]\{\cos(\pi z/z_T) - [z_T/(2\pi H)]\sin(\pi z/z_T)\}$, the vertical structure function for $\phi_t(r, z), v_t(r, z), u_t(r, z)$. The blue curve reaches a maximum value of approximately 1.596 at $z=z_m \approx 8.776$ km.

we can show that the hydrostatic, gradient wind, tangential wind, and thermodynamic equations respectively imply that

$$\frac{g}{T_0} \hat{T}_t(r) = -\frac{z_T}{\pi} \left(\frac{\pi^2}{z_T^2} + \frac{1}{4H^2} \right) \hat{\phi}_t(r), \quad (16)$$

$$\hat{v}_t(r) = \left(f + \frac{2v}{r} \right)^{-1} \frac{d\hat{\phi}_t(r)}{dr}, \quad (17)$$

$$\hat{u}_t(r) = -\hat{f}^{-2} \frac{d\hat{\phi}_t(r)}{dr}, \quad (18)$$

$$\hat{w}_t(r) = \frac{g}{T_0 N^2} \left(\frac{\hat{Q}(r)}{c_p} - \hat{T}_t(r) \right). \quad (19)$$

Substituting (14) and (15) into (11) we find that the ordinary differential equation for the radial structure of the temperature tendency is given by the top entry in (22), where

$$\ell(r) = \frac{N}{\hat{f}(r)} \left(\frac{\pi^2}{z_T^2} + \frac{1}{4H^2} \right)^{-1/2} = \frac{f}{\hat{f}(r)} \ell_0 \quad (20)$$

is the Rossby length. As $r \rightarrow \infty$, $\hat{f}(r) \rightarrow f$ and $\ell(r) \rightarrow \ell_0$, the constant far-field value which we shall assume is equal to 1000 km. One of the remarkable features of hurricanes is the wide range of $\ell(r)$, which can shrink from this far-field value of 1000 km to less than 10 km in the core.

[15] From the first entry in (13), the boundary condition at $r=0$ can be written as the second entry in (22). Since our problem is to be solved numerically over a finite domain, we need to replace the boundary condition $r\hat{T}_t \rightarrow 0$ as $r \rightarrow \infty$ with an approximate far-field boundary condition at some large radius $r=b$. In the far-field $\hat{Q} \rightarrow 0$ and $\ell(r) \rightarrow \ell_0$, so that the top line of (22) simplifies to

$$\frac{d^2 \hat{T}_t}{dr^2} + \frac{d\hat{T}_t}{r dr} - \frac{1}{\ell_0^2} \hat{T}_t = 0 \quad \text{for large } r. \quad (21)$$

The solution of (21) consists of a linear combination of the zero order modified Bessel functions, i.e., $\hat{T}_t(r) = AK_0(r/\ell_0) + BI_0(r/\ell_0)$, where A and B are constants. Since $I_0(r/\ell_0) \rightarrow \infty$ as $r \rightarrow \infty$, we require $B=0$, so that $\hat{T}_t(r) = AK_0(r/\ell_0)$ for large r . The value of A depends on the details of the solution in the inner region, but it can be eliminated by noting that $d\hat{T}_t/dr = -(A/\ell_0)K_1(r/\ell_0)$, so that, at $r=b$, $d\hat{T}_t/dr$ and \hat{T}_t are related by the third line in (22). In all the calculations shown here we have assumed $b=1000$ km and $\ell_0=1000$ km, so that the factor in the large parentheses on the right hand side of the third line in (22) is approximately (700 km^{-1}) .

[16] To summarize, the second order differential equation and the appropriate boundary conditions for our problem are

$$\begin{aligned} \hat{T}_t - \frac{d}{dr} \left(\ell^2 r \frac{d\hat{T}_t}{dr} \right) &= \frac{\hat{Q}}{c_p}, \\ \frac{d\hat{T}_t}{dr} &= 0 \quad \text{at } r=0, \\ \frac{d\hat{T}_t}{dr} &= - \left(\frac{K_1(b/\ell_0)}{\ell_0 K_0(b/\ell_0)} \right) \hat{T}_t \quad \text{at } r=b. \end{aligned} \quad (22)$$

Once $\hat{T}_t(r)$ is found from (22), the original fields $T_t(r,z)$, $v_t(r,z)$, $\phi_t(r,z)$, $u(r,z)$, and $w(r,z)$ can be recovered from (14)–(19). Solutions of (22) reveal how the nonlocal relationship between the diabatic heating $\hat{Q}(r)$ and the temperature tendency $\hat{T}_t(r)$ is modulated by the vortex structure through the radial distribution of the Rossby length $\ell(r)$. Understanding the nonlocal behavior of the solutions of (22) is a crucial part of an overall understanding of the rapid intensification process. *Vigh and Schubert* [2009] have solved (22) analytically for the special case in which $\ell(r)$ is piecewise constant over two regions—the core and the far-field. They have shown that, when $\hat{Q}(r)$ is localized in a region where $\ell(r)$ is small, it is possible for $\hat{T}_t(r)$ to be large and localized in the same region because the small values of $\ell(r)$ reduce the magnitude of the second derivative term even though $|d^2\hat{T}_t/dr^2|$ is large. In the present study we consider radial profiles of $\ell(r)$ that are more complicated, i.e., profiles that have low values of $\ell(r)$ in the core, large values of $\ell(r)$ in the far-field, but a more gradual transition due to the presence of a “vorticity skirt” outside the radius of maximum wind. Because of these more complicated radial profiles of $\ell(r)$, we shall solve (22) numerically.

[17] If the differential equation in the top line of (22) were solved on an infinite domain with the boundary condition $r\hat{T}_t \rightarrow 0$ as $r \rightarrow \infty$, then integration of this differential equation would yield the integral relation

$$\int_0^\infty \hat{T}_t r dr = \int_0^\infty \frac{\hat{Q}}{c_p} r dr, \quad (23)$$

which states that the area-integrated temperature tendency is equal to the area-integrated diabatic heating, even though $\hat{Q}(r)$ can be large and localized while $\hat{T}_t(r)$ can be small and spread over a wide area. What is the analogue of (23) for our finite domain? Integration of the differential equation over the computational domain $0 \leq r \leq b$, with use of the boundary conditions in (22), yields

$$\int_0^b \hat{T}_t r dr + \frac{\ell_0 b K_1(b/\ell_0)}{K_0(b/\ell_0)} \hat{T}_t(b) = \int_0^b \frac{\hat{Q}}{c_p} r dr, \quad (24)$$

where we have assumed that b is large enough that $\ell(b) \approx \ell_0$. Although our numerical solution for $\hat{T}_t(r)$ is obtained in the region $0 \leq r \leq b$, suppose we extend it to infinity by

$$\hat{T}_t(r) = \hat{T}_t(b) \frac{K_0(r/\ell_0)}{K_0(b/\ell_0)} \quad \text{for } b \leq r < \infty. \quad (25)$$

Integrating (25) we obtain

$$\begin{aligned} \int_b^\infty \hat{T}_t r dr &= \frac{\hat{T}_t(b)}{K_0(b/\ell_0)} \int_b^\infty K_0(r/\ell_0) r dr \\ &= - \frac{\ell_0 \hat{T}_t(b)}{K_0(b/\ell_0)} \int_b^\infty \frac{d[rK_1(r/\ell_0)]}{dr} dr \\ &= \frac{\ell_0 b K_1(b/\ell_0)}{K_0(b/\ell_0)} \hat{T}_t(b). \end{aligned} \quad (26)$$

Since the right hand side of (26) is equal to the second term in (24), and since we have assumed that $\hat{Q} = 0$ for $b \leq r < \infty$, we can simplify (24) to

$$\int_0^b \hat{T}_t r dr + \int_b^\infty \hat{T}_t r dr = \int_0^\infty \frac{\hat{Q}}{c_p} r dr, \quad (27)$$

which is equivalent to the infinite domain result (23). Thus, in the sense that the finite domain result is extended to infinity according to (25), the integral relation (23) is preserved.

3. Effect of a Vorticity Skirt on the Intensification Rate

[18] We now consider some sample solutions of (22). In order to specify the $\ell(r)$ factor in (22), we consider the vortex

$$v(r) = \frac{\Gamma}{2\pi r} \left[1 - \exp\left(-\frac{r^2}{a^2}\right) \right], \quad (28)$$

where Γ and a are constants. The maximum wind is $v_{\max} \approx 0.6382\Gamma/(2\pi a)$, which occurs at $r_{\max} \approx 1.121a$. Since $2\pi r v \rightarrow \Gamma$ as $r \rightarrow \infty$, the constant Γ represents the circulation at large radii. The relative vorticity field associated with (28) is given by

$$\zeta(r) = \frac{d(rv)}{r dr} = \frac{\Gamma}{\pi a^2} \exp\left(-\frac{r^2}{a^2}\right), \quad (29)$$

so the constant a is the e -folding radius of the vorticity distribution. Using (28) and (29) in (10), we obtain

$$\begin{aligned} \hat{f}^2(r) &= \left\{ f + \frac{\Gamma}{\pi r^2} \left[1 - \exp\left(-\frac{r^2}{a^2}\right) \right] \right\} \\ &\quad \cdot \left\{ f + \frac{\Gamma}{\pi a^2} \exp\left(-\frac{r^2}{a^2}\right) \right\}, \end{aligned} \quad (30)$$

from which $\ell(r)$ can be computed using (20). For the results presented in this section we have chosen $a = 26.76$ km and $\Gamma = 7.905 \times 10^6 \text{ m}^2 \text{ s}^{-1}$, which corresponds to $r_{\max} \approx 30$ km and $v_{\max} \approx 30 \text{ m s}^{-1}$. Figure 7 shows $v(r)$, $\zeta(r)$, and $\ell(r)$ profiles for this vortex. Note that the maximum vorticity is approximately $70f$ (for $f = 5 \times 10^{-5} \text{ s}^{-1}$) and that the Rossby length is less than 20 km in the vortex core but begins to increase rapidly toward its far-field value outside a radius of 50 km.

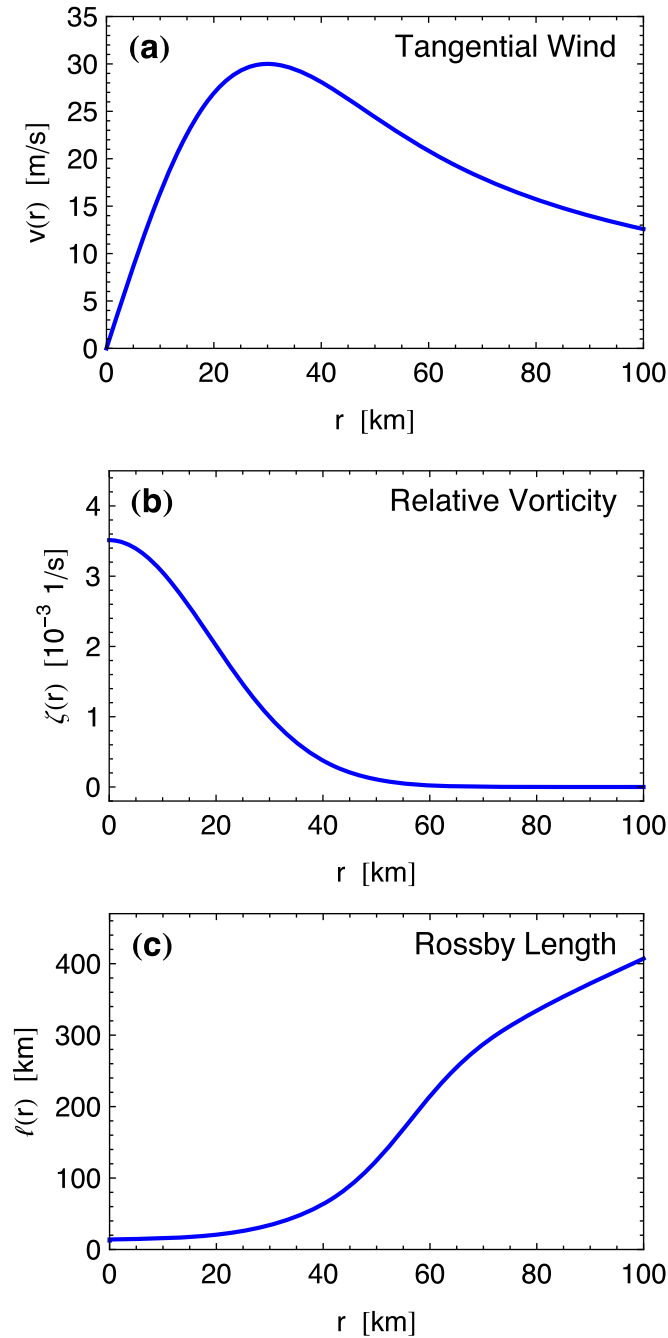


Figure 7. Radial profiles of (a) tangential wind $v(r)$, (b) relative vorticity $\zeta(r)$, and (c) Rossby length $\ell(r)$ for the Gaussian vortex defined by (28), with the constants Γ and a chosen such that the wind maximum is 30 m s^{-1} at a radius of 30 km.

[19] To specify the $\hat{Q}(r)$ term in (22) we assume that the diabatic heating has the form of an annular ring with smooth edges. A plausible explanation for the diabatic heating taking the form of an annular ring has been provided by *Eliassen* [1971] and *Eliassen and Lystad* [1977], who showed that the Ekman pumping at the top of a turbulent boundary layer under an axisymmetric vortex vanishes at the vortex center and reaches a maximum at a certain distance from the vortex center [see also *Yamasaki*, 1977; *Emanuel*,

1997; *Smith and Vogl*, 2008; *Smith and Montgomery*, 2008; *Kepert*, 2010a, 2010b]. This result, which arises from the use of a stress condition at the top of the thin surface Prandtl layer, is qualitatively different from the more radially uniform Ekman pumping at the top of a laminar boundary layer that uses a no-slip condition at the surface. Although our dynamical model (1)–(5) does not explicitly contain Ekman layer effects, we use these conceptual notions to justify the specification

$$\hat{Q}(r) = \hat{Q}_{\text{ew}} \begin{cases} 0 & 0 \leq r \leq r_1, \\ S\left(\frac{r_2-r}{r_2-r_1}\right) & r_1 \leq r \leq r_2, \\ 1 & r_2 \leq r \leq r_3, \\ S\left(\frac{r-r_3}{r_4-r_3}\right) & r_3 \leq r \leq r_4, \\ 0 & r_4 \leq r < \infty, \end{cases} \quad (31)$$

where $S(s)=1-3s^2+2s^3$ is the cubic interpolating function satisfying $S(0)=1$, $S(1)=0$, $S'(0)=S'(1)=0$, and r_1, r_2, r_3, r_4 are specified constants. The eyewall diabatic heating, denoted by \hat{Q}_{ew} , is determined from r_1, r_2, r_3, r_4 by imposing the constraint that the total diabatic heating is fixed, i.e.,

$$2\pi \int_0^{r_4} \frac{\hat{Q}(r)}{c_p} r dr = (3.2 \text{ K day}^{-1}) \cdot \pi (250 \text{ km})^2. \quad (32)$$

Fixing the total diabatic heating is essentially the same as fixing the total rainfall or fixing the diabatic generation of total energy, as can be seen from (6). For further discussion of this normalization technique, see *Schubert and Hack* [1982], especially their Table 1, which is based on the observational analysis of *Gray* [1981]. Substituting (31) into (32), and performing the integration, we obtain

$$\frac{\hat{Q}_{\text{ew}}}{c_p} = G \cdot (3.2 \text{ K day}^{-1}), \quad (33)$$

where the dimensionless geometrical factor G is given by

$$G = \frac{10(250 \text{ km})^2}{(3r_3^2 + 4r_3r_4 + 3r_4^2) - (3r_1^2 + 4r_1r_2 + 3r_2^2)}. \quad (34)$$

Note that $G=1$ in the special case $r_1=r_2=0$ and $r_3=r_4=250$ km, in which case the peak value of the diabatic heating occurs at $z=8.776$ km (see Figure 6) and has the value $\hat{Q}/c_p = (1.596) \cdot (3.2 \text{ K day}^{-1}) = 5.107 \text{ K day}^{-1}$, a value typical of western Pacific convective cloud cluster regions [*Yanai et al.*, 1973]. For general eyewall patterns of heating, we can compute \hat{Q}_{ew} from (33) and (34) once r_1, r_2, r_3, r_4 are specified. Plots of $\hat{Q}(r)/c_p$, computed using the parameters listed in Table 1, are shown in Figure 8. The cases can be described as follows. In H1 the heating lies well outside the radius of maximum wind and at the outer edge of the vorticity skirt. In H2 the heating

Table 1. Bounding Radii r_1, r_2, r_3, r_4 and the Factor G for the Four $\hat{Q}(r)/c_p$ Profiles Shown in Figure 8

Case	r_1 (km)	r_2 (km)	r_3 (km)	r_4 (km)	G
H1	40	45	55	60	41.67
H2	30	35	45	50	52.08
H3	20	25	35	40	69.44
H4	10	15	25	30	104.17

lies just outside the radius of maximum wind and is partially inside the vorticity skirt. In H3 the heating extends across the radius of maximum wind and thus lies in a region of rapidly changing inertial stability and Rossby length. In H4 the heating is confined inside the radius of maximum wind, so that all the heating is in a region of high inertial stability and small Rossby length. Note that the constraint (32), together with the assumed vertical structure of $Q(r, z)$ given by (14), means that the total energy generation given by the right hand side of (6) is the same for each heating profile shown in Figure 8. However, the fraction of the total energy generation that is partitioned to kinetic energy generation is dependent on the position of the diabatic heating relative to the inertial stability. An “energetic efficiency” interpretation of this effect has been given by *Hack and Schubert* [1986].

[20] The results of the first three heating profiles H1, H2, H3 are shown in Figures 9–11 respectively. Figures 9a–11a show the tangential wind $v(r)$ in blue, the relative vorticity $\zeta(r)$ in red, and the diabatic heating $\hat{Q}(r)$ in gray shading, Figures 9b–11b show the temperature tendency $\hat{T}_t(r)$, Figures 9c–11c show the geopotential tendency $\hat{\phi}_t(r)$, Figures 9d–11d show the radial flow $\hat{u}(r)$ in blue and the vertical velocity $\hat{w}(r)$ in red, Figure 9e–11e show the tangential wind $v(r)$ in blue, the surface tangential wind tendency $v_t(r, 0)$ in red, and the resulting surface tangential wind $v(r) + v_t(r, 0) \cdot 6 \text{ h}$ in green, and finally Figures 9f–11f show the vorticity $\zeta(r)$ in blue, the surface vorticity tendency $\zeta_t(r, 0)$ in red, and the resulting surface vorticity $\zeta(r) + \zeta_t(r, 0) \cdot 6 \text{ h}$ in green. In all three cases the vertical velocity is upward in the diabatically heated region and weakly downward outside this region. The radial flow is weak and outward near the inside edge of the heating, while it is stronger and inward near the outside edge of the heating. The radius where $u=0$ is not near the center of the diabatically forced region but rather lies very near the inner edge of that region. In other words, the radial flow is inward over nearly the entire diabatically forced region, so that $\hat{v}_t = -(f + \zeta)\hat{u} > 0$ over nearly the entire diabatically forced region. Because of the radial variation of $f + \zeta$, the tangential wind tendency $\hat{v}_t(r)$ does not peak at the same radius where the inflow

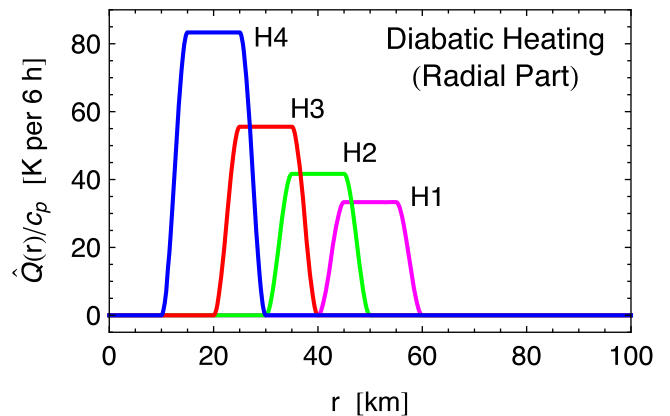


Figure 8. Radial profiles of diabatic heating $\hat{Q}(r)/c_p$ for the cases listed in Table 1.

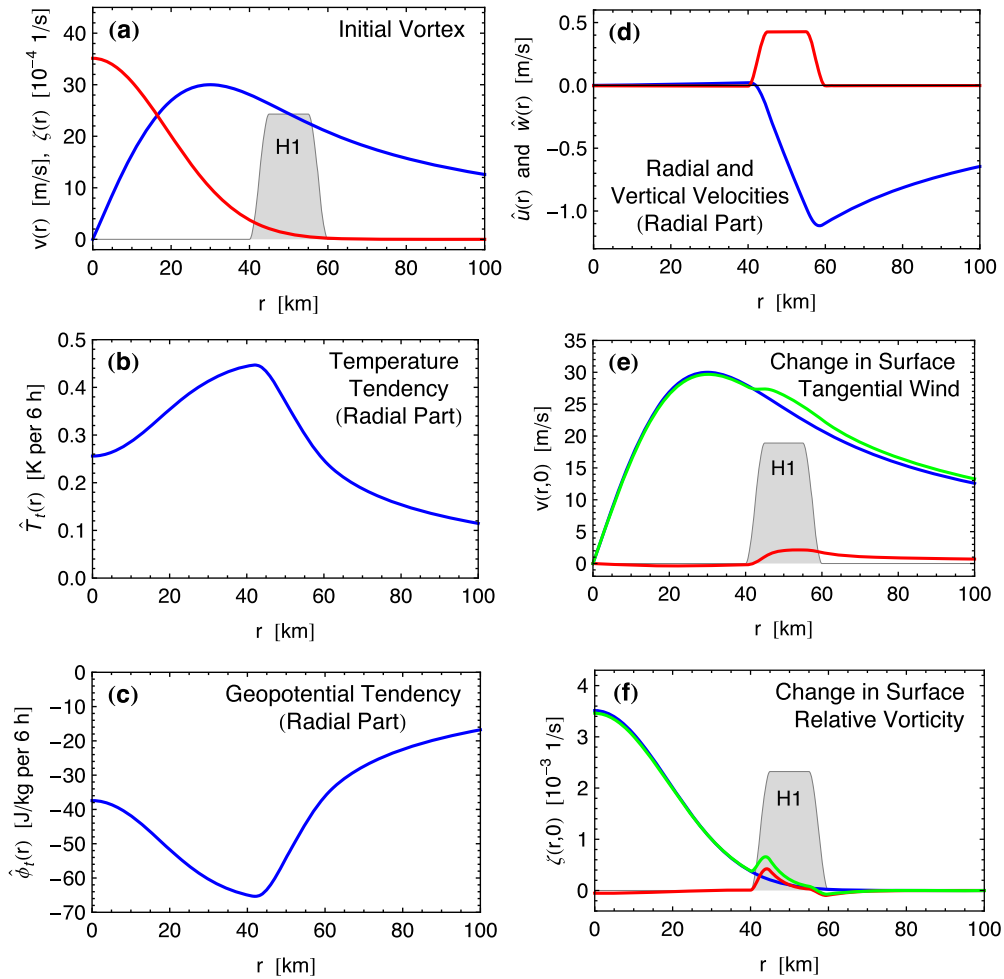


Figure 9. Changes in vortex structure for case H1, where the diabatic heating occurs well outside the radius of maximum wind: (a) radial profiles of tangential wind $v(r)$ in blue, relative vorticity $\zeta(r)$ in red, and (arbitrarily scaled) diabatic heating $Q(r)$ in gray shading; (b) radial profile of the temperature tendency $\hat{T}_t(r)$; (c) radial profile of the geopotential tendency $\hat{\phi}_t(r)$; (d) radial profile of the secondary circulation, with the radial wind $\hat{u}(r)$ in blue and the vertical velocity $\hat{w}(r)$ in red; (e) radial profile of the initial tangential wind $v(r)$ in blue, the tangential wind tendency $\hat{v}_t(r)$ in red with units of $\text{m s}^{-1} (\text{6 h})^{-1}$, and the surface tangential wind after six hours in green; (f) radial profile of the initial relative vorticity $\zeta(r)$ in blue, the vorticity tendency $\zeta_t(r,0)$ in red with units of $10^{-3} \text{ s}^{-1} (\text{6 h})^{-1}$, and surface relative vorticity after six hours in green. For reference, the (arbitrarily scaled) diabatic heating is also shown in Figures 9e and 9f.

peaks, i.e., $\hat{v}_t(r)$ generally peaks closer to the center of the heating. In all cases the tendencies of temperature, geopotential, and vorticity are maximized along the inner edge of the heating profile. Case H1 (Figure 9) illustrates the tendency for diabatic heating at the outer edge of the vorticity skirt to increase the outer tangential winds while having a minimal effect on the inner winds, corresponding to the early mature stage in Figure 3. For case H2 (Figure 10), the heating is just outside the radius of maximum wind, i.e., in the region of the vorticity skirt. This is more efficient than case H1, with the tangential winds increasing at a rate of approximately $1.1 \text{ m s}^{-1} \text{ h}^{-1}$, corresponding to the developing stage in Figure 3. For case H3 an intense response is seen (Figure 11). The tangential wind tendency is approximately $3 \text{ m s}^{-1} \text{ h}^{-1}$, with the maximum located just inside the inflow maximum and just outside the original radius of maximum wind. The vortex

expands slightly as it intensifies, and the vortex profile inside the heating hollows [Shapiro and Willoughby, 1982; Kossin and Eastin, 2001]. Note that the maximum intensification rates found by Zehr and Knaff [2007] for major Atlantic hurricanes are in the range 1 to $2 \text{ m s}^{-1} \text{ h}^{-1}$, so the tendency found in case H3 should be regarded as near the upper limit of observed values.

[21] We have also calculated solutions for the case H4 (not shown). In this case the diabatic heating lies entirely within the radius of maximum wind, where the vorticity is largest and the local Rossby length is smallest. The tangential wind tendencies in case H4 are so large ($\sim 9 \text{ m s}^{-1} \text{ h}^{-1}$) that they correspond to intensification rates that have apparently never been observed. One interpretation of this result is that certain physical processes (e.g., boundary layer frictional effects) do not allow the diabatic heating field to occur entirely within the radius

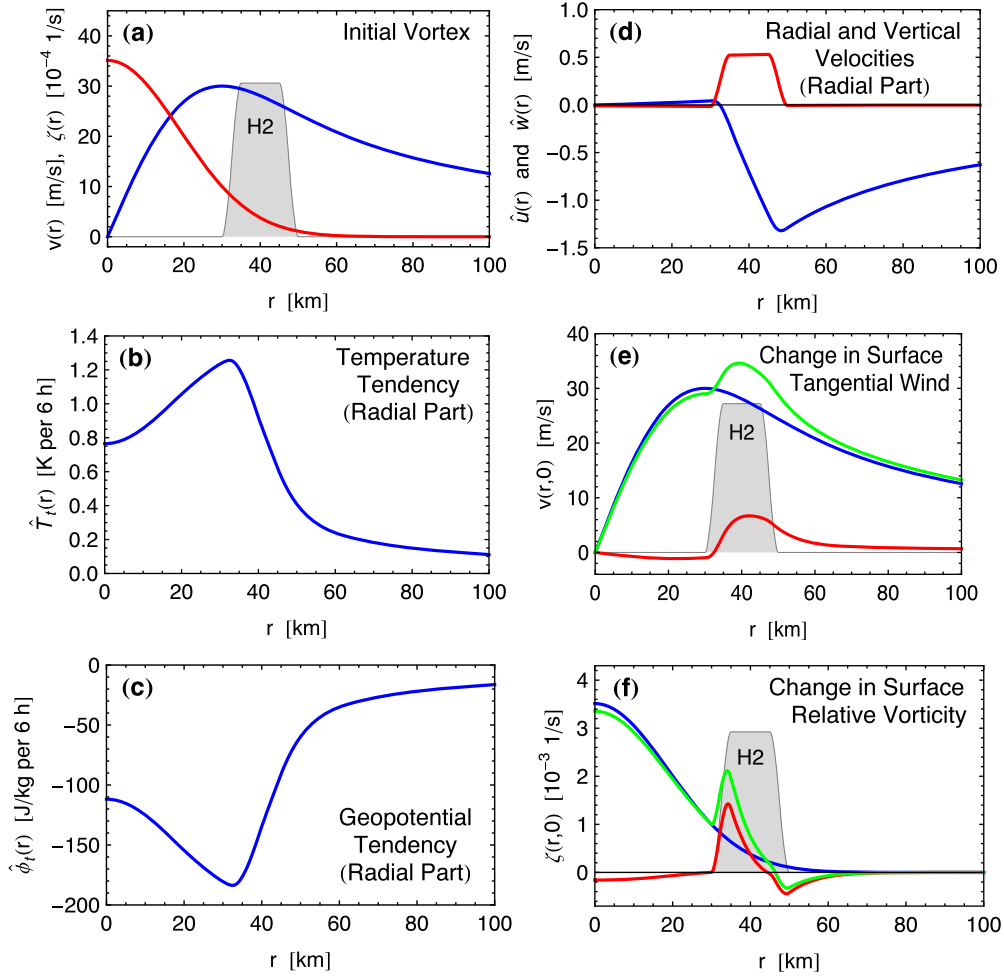


Figure 10. Same as Figure 9, but changes in vortex structure for case H2, where the diabatic heating occurs just outside the radius of maximum wind.

of maximum wind for a vortex of this strength. In any event, this example illustrates the hypersensitivity of the intensification rate to the location of the diabatic heating relative to the high vorticity core. The results presented in this section are consistent with our previous interpretation (see section 1) of Figure 1, i.e., the rapid intensification period in the top and bottom panels of Figure 1 occurs when the diabatic heating (indicated by the r of max w) is closest to the radius of maximum wind. In contrast, when the diabatic heating is well outside the radius of maximum wind (as in Figure 9), the maximum wind does not change but the outer winds and therefore the integrated kinetic energy increase, as occurs for $132 \leq t \leq 144$ h in Figure 3.

4. Effect of Vorticity Skirts of Different Widths

[22] In the previous section we examined the balanced response of a 30 m s^{-1} vortex to diabatic heating in four different annular regions. In this section we examine the balanced response of five different vortices to a fixed diabatic heating, which is again specified according to (31)–(34), but now with $(r_1, r_2, r_3, r_4) = (20, 30, 40, 50)$ km. Each vortex has a constant relative vorticity in the core

region and zero relative vorticity in the far-field, with a smooth transition between the two regions. The mathematical form for the relative vorticity $\zeta = d(rv)/rdr$ is

$$\zeta(r) = \zeta_0 \begin{cases} 1 & 0 \leq r \leq \hat{r}_1, \\ S\left(\frac{r - \hat{r}_1}{\hat{r}_2 - \hat{r}_1}\right) & \hat{r}_1 \leq r \leq \hat{r}_2, \\ 0 & \hat{r}_2 \leq r < \infty, \end{cases} \quad (35)$$

where $S(s)$ is the same cubic interpolating function used previously, \hat{r}_1, \hat{r}_2 are specified constants, and the core vorticity ζ_0 is given by

$$\zeta_0 = \frac{10\Gamma}{\pi(3\hat{r}_1^2 + 4\hat{r}_1\hat{r}_2 + 3\hat{r}_2^2)}, \quad (36)$$

with $\Gamma = 2\pi \times 10^6 \text{ m}^2 \text{ s}^{-1}$ denoting the constant far-field circulation. Figure 12b shows five such $\zeta(r)$ profiles, all having $\hat{r}_1 = 20$ km and with $\hat{r}_2 = 30, 40, 50, 60, 70$ km. The associated $v(r)$ and $\ell(r)$ profiles are shown in Figures 12a and 12c. For the blue and red cases, the vorticity skirt and the associated small values of $\ell(r)$ extend part way

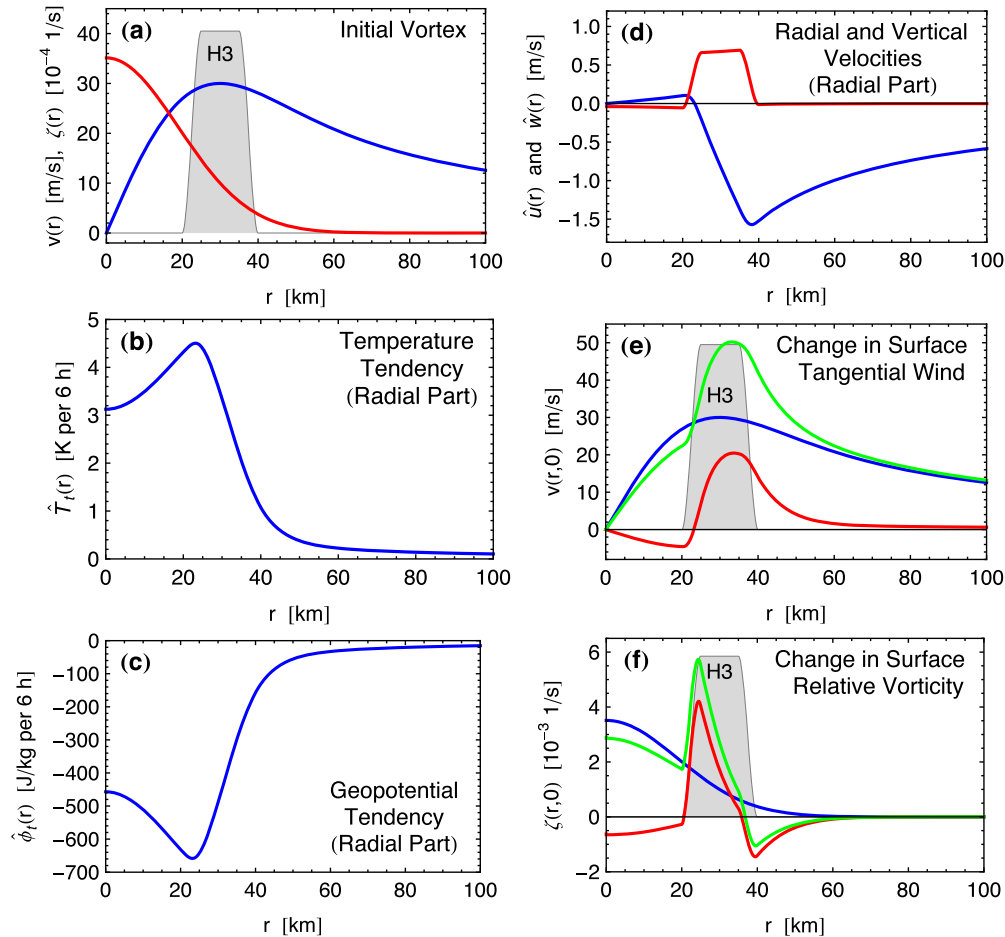


Figure 11. Same as Figure 9, but changes in vortex structure for case H3, where the diabatic heating extends across the radius of maximum wind.

into the diabatically heated region, while for the cyan and magenta cases, the vorticity skirt and small values of $\ell(r)$ extend across and beyond the diabatically heated region. Note that all the $v(r)$ profiles are identical outside a radius of 70 km (e.g., all have 10 m s^{-1} winds at 100 km), so that the average vorticity inside 70 km is the same for all profiles.

[23] The tangential wind tendencies $\hat{v}_t(r)$ and the temperature tendencies $\hat{T}_t(r)$ are shown in Figures 12e and 12f. Note the general reversal of the ordering, i.e., the smallest tendencies are found for the vortex with the strongest tangential wind (37 m s^{-1}), while the largest tendencies tend to be found for the vortex with the weakest tangential wind (17 m s^{-1}). Figure 12d shows the surface tangential winds after 6 h. These results demonstrate the crucial importance of the location of the heating within the vorticity skirt. Although the 37 m s^{-1} vortex has high inertial stability and small Rossby length in its core, its potential for rapid development remains untapped because most of the diabatic heating lies outside the vorticity skirt in a region of larger Rossby lengths.

[24] The results displayed in Figure 12 illustrate the simultaneous production of warm rings and U-shaped wind profiles, where a U-shaped wind profile is defined as

a tangential wind profile in which the wind is weak in the central part of the vortex but increases rapidly with radius near the inner edge of the eyewall. For such profiles the vorticity (and potential vorticity) is largest in an annular ring, which means that the radial gradient of vorticity has both signs and the Rayleigh necessary condition for barotropic instability is satisfied (i.e., there are counter-propagating Rossby waves). However, if the annular ring is wide enough (e.g., the inner radius of the ring is less than half the outer radius of the ring), the flow tends to be exponentially stable [see *Schubert et al.*, 1999, Figures 1 and 2]. Exponential instability occurs for thin rings, and, at finite amplitude, the instability is associated with the inward mixing of high vorticity. How are U-shaped wind profiles produced? The results of Figure 12d indicate that U-shaped wind profiles tend to be produced when part of the diabatic heating occurs just inside the radius of maximum wind.

5. Concluding Remarks

[25] As a simple way to interpret the behavior of tropical cyclones on a K - V_{\max} diagram we have derived the idealized boundary value problem (22), which relates the diabatic heating $\hat{Q}(r)$, the Rossby length $\ell(r)$, and the

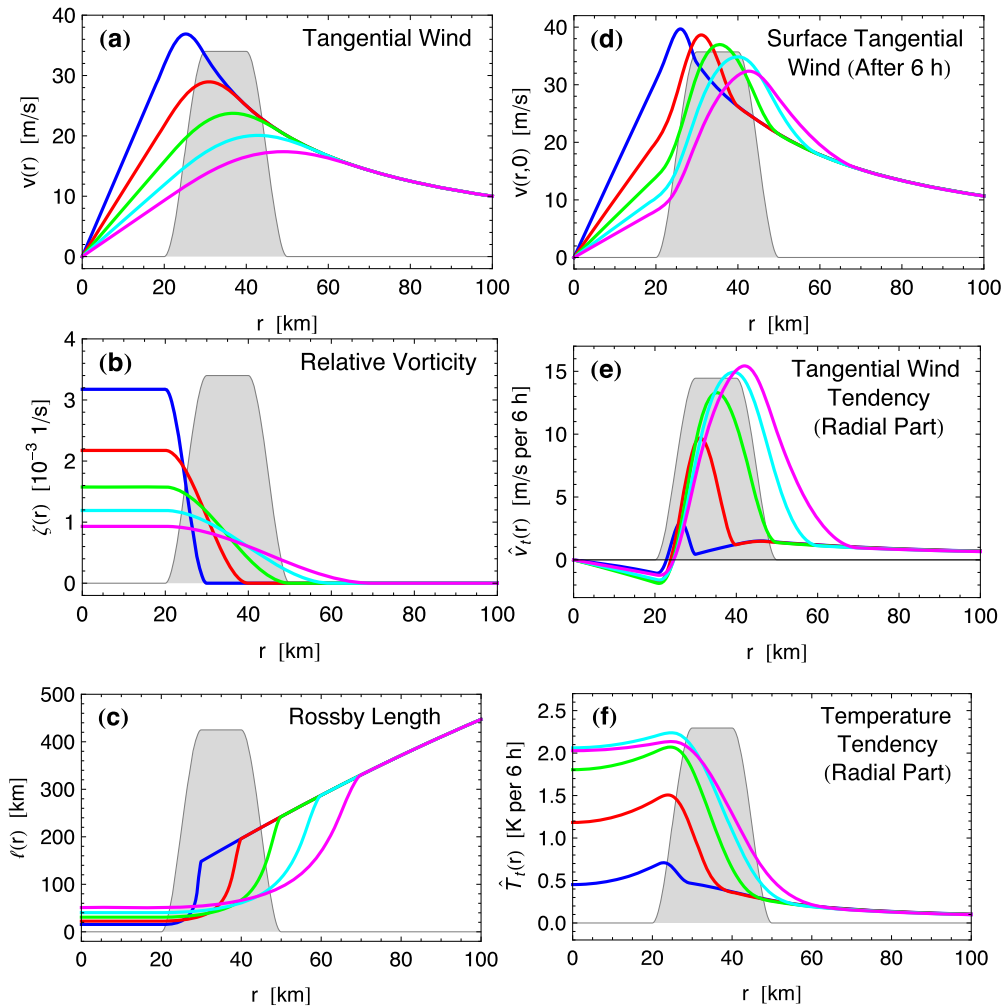


Figure 12. (b) Five $\zeta(r)$ profiles computed from (35). All five profiles have $\hat{r}_1 = 20$ km, and have $\hat{r}_2 = 30, 40, 50, 60, 70$ km. (a, c) The associated $v(r)$ and $\ell(r)$ profiles are shown. (e, f) The tendencies $\hat{v}_t(r)$ and $\hat{T}_t(r)$ are shown, and (d) the surface tangential wind after 6 hours is shown. The shaded region between 20 km and 50 km is the diabatically heated region (arbitrarily scaled).

radial distribution of the mass field tendency $\hat{T}_t(r)$ (or equivalently, through gradient balance, the tangential wind tendency $\hat{v}_t(r)$). We have shown that one of the crucial factors for rapid intensification of a tropical cyclone is the occurrence of deep convection in a region of small Rossby length. In particular, if the tropical cyclone has a Gaussian-like vorticity structure, with large vorticity (and small Rossby length) in the core and decreasing vorticity (with increasing Rossby length) in the skirt, then rapid intensification will not occur unless some of the deep convection occurs well within the skirt. Observations of the three-dimensional distribution of vorticity in a tropical cyclone are very difficult to obtain. This fact, along with the theoretical results presented here, indicate that intensity forecasting is fundamentally more difficult than track forecasting because the intensification rate depends not just on the average vorticity inside 100 km, but also on the details of the vorticity distribution in this inner core region.

[26] Some of the issues we have explored here in the context of the balanced vortex model have also been

recently explored in the context of full physics models, especially the issue of the wide range in tropical cyclone sizes. These studies have clarified the important role of diabatic heating outside the eyewall and in the outer spiral rainbands [Wang, 2009; Xu and Wang, 2010a; Fudeyasu and Wang, 2011], the role of the initial vortex size [Xu and Wang, 2010b], the role of eyewall tilt [Wang, 2008; Pendergrass and Willoughby, 2009], and the role of environmental humidity, with dry environments leading to smaller storms [Hill and Lackmann, 2009].

[27] K - V_{\max} diagrams such as the one shown in Figure 3 are presently finding practical use in operational weather analysis and forecasting. They would also appear to be useful to theoreticians and numerical modelers as a way to summarize the life cycles of model tropical cyclones. For example, they would be a convenient way to summarize some of the variability found in ensemble forecasts of tropical cyclone intensity.

[28] Although the inviscid, axisymmetric, balanced model presented here (and further in Musgrave [2011]) is highly idealized, it is possible that the general concepts

developed from it can be useful in statistical hurricane intensity prediction schemes such as those discussed by DeMaria *et al.* [2001, 2005, 2007], Kaplan and DeMaria [2003], Knaff *et al.* [2003b], Elsberry *et al.* [2007], and Kaplan *et al.* [2010]. Research with this goal is currently underway.

Appendix A: Solution of the Radial Structure Equation Using Mathematica

[29] The problem (22) is solved using NDSolve, which is the numerical differential equation solver in the Mathematica software package. NDSolve can solve single ordinary differential equations, sets of simultaneous ordinary differential equations, and some partial differential equations, although not the elliptic equation (11). NDSolve finds solutions iteratively, adapting its step size to the accuracy and precision goals of the user. In fact, a large number of options are available, through which the user can control not only accuracy and precision, but also such details as the particular discretization method. For ordinary differential equations, NDSolve by default uses the LSODE (Livermore Solver for Ordinary Differential Equations) approach, which switches between a non-stiff Adams method and a stiff Gear backward difference method. For linear boundary value problems, such as the one solved here, NDSolve uses the Gel'fand-Lokutsiyevskii chasing method, which is effectively a shooting method that uses linearity to good advantage. The robustness of this Mathematica tool for solving a wide variety of problems is obtained at the cost of considerable complexity, with the code for NDSolve and related functions totaling approximately 1400 pages. To prepare (22) for solution by NDSolve, we first put the differential equation in the form

$$\frac{d^2 \hat{T}_t}{dr^2} + \left(\frac{1}{r} + \frac{d \ln(\ell^2)}{dr} \right) \frac{d \hat{T}_t}{dr} - \frac{1}{\ell^2} \hat{T}_t = - \frac{1}{\ell^2} \frac{\hat{Q}}{c_p}. \quad (\text{A1})$$

Note that (A1) reduces to the zero order modified Bessel equation in the far-field, where $\ell(r) \rightarrow \ell_0$ and $\hat{Q}(r) \rightarrow 0$, which serves as the motivation for the $r=b$ boundary condition in (22). The domain for the radial structure equation (A1) is ideally $0 \leq r \leq b$. However, because of the singularity at $r=0$, we have numerically solved (A1) on the domain $a \leq r \leq b$, where we have chosen a to be very small (10^{-16} m). The Mathematica notebook used for the calculations presented here is included on the journal website as supplementary material¹ to this article.

[30] **Acknowledgments.** We would like to thank Paul Ciesielski, Chris Davis, Mark DeMaria, Richard Johnson, Michael Kirby, David Randall, Russ Schumacher, and David Thompson for their helpful comments. We would also like to thank Yuqing Wang and an anonymous reviewer for their insightful reviews of this paper. This research was supported by National Oceanographic Partnership

Program through ONR contract N00014-10-1-0145, and the National Science Foundation under grant ATM-0837932 and under the Science and Technology Center for Multi-Scale Modeling of Atmospheric Processes, managed by Colorado State University through cooperative agreement ATM-0425247. This work was performed on high-end Linux workstations generously provided through a gift from the Hewlett-Packard Corporation.

References

- Arakawa, H. (1952), Mame Taifu or midget typhoon (small storms of typhoon intensity), *Geophys. Mag.*, *24*, 463–474.
- Brand, S. (1972), Very large and very small typhoons of the western North Pacific Ocean, *J. Meteorol. Soc. Jpn.*, *50*, 332–341.
- Bui, H. H., R. K. Smith, M. T. Montgomery, and J. Peng (2009), Balanced and unbalanced aspects of tropical cyclone intensification, *Q. J. R. Meteorol. Soc.*, *135*, 1715–1732, doi:10.1002/qj.502.
- Corbosiero, K. L., J. Molinari, and M. L. Black (2005), The structure and evolution of Hurricane Elena (1985). Part I: Symmetric intensification, *Mon. Weather Rev.*, *133*, 2905–2921, doi:10.1175/MWR3010.1.
- DeMaria, M., J. A. Knaff, and B. H. Connell (2001), A tropical cyclone genesis parameter for the tropical Atlantic, *Weather Forecast.*, *16*, 219–233, doi:10.1175/1520-0434(2001)016<0219:ATCGPF>2.0.CO;2.
- DeMaria, M., M. Mainelli, L. K. Shay, J. A. Knaff, and J. Kaplan (2005), Further improvements to the Statistical Hurricane Intensity Prediction Scheme (SHIPS), *Weather Forecast.*, *20*, 531–543, doi:10.1175/WAF862.1.
- DeMaria, M., J. A. Knaff, and C. Sampson (2007), Evaluation of long-term trends in tropical cyclone intensity forecasts, *Meteorol. Atmos. Phys.*, *97*, 19–28, doi:10.1007/s00703-006-0241-4.
- Didlake, A. C., and R. A. Houze (2011), Kinematics of the secondary eyewall observed in Hurricane Rita (2005), *J. Atmos. Sci.*, *68*, 1620–1636, doi:10.1175/2011JAS3715.1.
- Dunnavan, G. M., and J. W. Diercks (1980), An analysis of Super Typhoon Tip (October 1979), *Mon. Weather Rev.*, *108*, 1915–1923, doi:10.1175/1520-0493(1980)108<1915:AAOSTT>2.0.CO;2.
- Eliassen, A. (1971), On the Ekman layer in a circular vortex, *J. Meteorol. Soc. Jpn.*, *49*, 784–789.
- Eliassen, A., and M. Lystad (1977), The Ekman layer of a circular vortex—A numerical and theoretical study, *Geophys. Norv.*, *31*, 1–16.
- Elsberry, R., T. D. B. Lambert, and M. A. Boothe (2007), Accuracy of Atlantic and eastern North Pacific tropical cyclone intensity forecast guidance, *Weather Forecast.*, *22*, 747–762, doi:10.1175/WAF1015.1.
- Emanuel, K. A. (1997), Some aspects of hurricane inner-core dynamics and energetics, *J. Atmos. Sci.*, *54*, 1014–1026, doi:10.1175/1520-0469(1997)054<1014:SAOHIC>2.0.CO;2.
- Fudeyasu, H., and Y. Wang (2011), Balanced contribution to the intensification of a tropical cyclone simulated in TCM4: Outer-core spinup process, *J. Atmos. Sci.*, *68*, 430–449, doi:10.1175/2010JAS3523.1.
- Gray, W. M. (1981), *Recent Advances in Tropical Cyclone Research from Rawinsonde Composite Analysis*, 407 pp., World Meteorol. Organ., Geneva, Switzerland.
- Hack, J. J., and W. H. Schubert (1986), Nonlinear response of atmospheric vortices to heating by organized cumulus convection, *J. Atmos. Sci.*, *43*, 1559–1573, doi:10.1175/1520-0469(1986)043<1559:NROAVT>2.0.CO;2.
- Harr, P. A., M. S. Kalafsky, and R. L. Elsberry (1996), Environmental conditions prior to formation of a midget tropical cyclone during TCM-93, *Mon. Weather Rev.*, *124*, 1693–1710, doi:10.1175/1520-0493(1996)124<1693:ECPTFO>2.0.CO;2.
- Hawkins, H. F., and S. M. Imbembro (1976), The structure of a small, intense hurricane—Inez 1966, *Mon. Weather Rev.*, *104*, 418–442, doi:10.1175/1520-0493(1976)104<0418:TSOASI>2.0.CO;2.
- Hendricks, E. A., and W. H. Schubert (2010), Adiabatic rearrangement of hollow PV towers, *J. Adv. Model. Earth Syst.*, *2*, 8, doi:10.3894/JAMES.2010.2.8.
- Hendricks, E. A., W. H. Schubert, R. K. Taft, H. Wang, and J. P. Kossin (2009), Life cycles of hurricane-like vorticity rings, *J. Atmos. Sci.*, *66*, 705–722, doi:10.1175/2008JAS2820.1.
- Hill, K. A., and G. M. Lackmann (2009), Influence of environmental humidity on tropical cyclone size, *Mon. Weather Rev.*, *137*, 3294–3315, doi:10.1175/2009MWR2679.1.

¹Auxiliary materials are available in the HTML. doi:10.1029/2011MS001014

- Houze, R. A., S. Chen, B. F. Smull, W.-C. Lee, and M. M. Bell (2007), Hurricane intensity and eyewall replacement, *Science*, *315*, 1235–1239, doi:10.1126/science.1135650.
- Kaplan, J., and M. DeMaria (2003), Large-scale characteristics of rapidly intensifying tropical cyclones in the North Atlantic basin, *Weather Forecast.*, *18*, 1093–1108, doi:10.1175/1520-0434(2003)018<1093:LCORIT>2.0.CO;2.
- Kaplan, J., M. DeMaria, and J. A. Knaff (2010), A revised tropical cyclone rapid intensification index for the Atlantic and Eastern North Pacific Basins, *Weather Forecast.*, *25*, 220–241, doi:10.1175/2009WAF2222280.1.
- Keper, J. D. (2010a), Slab- and height-resolving models of the tropical cyclone boundary layer. Part I: Comparing the simulations, *Q. J. R. Meteorol. Soc.*, *136*, 1686–1699, doi:10.1002/qj.667.
- Keper, J. D. (2010b), Slab- and height-resolving models of the tropical cyclone boundary layer. Part II: Why the simulations differ, *Q. J. R. Meteorol. Soc.*, *136*, 1700–1711, doi:10.1002/qj.685.
- Knaff, J. A., J. P. Kossin, and M. DeMaria (2003a), Annular hurricanes, *Weather Forecast.*, *18*, 204–222, doi:10.1175/1520-0434(2003)018<0204:AH>2.0.CO;2.
- Knaff, J. A., M. DeMaria, J. Kaplan, C. R. Sampson, and J. M. Gross (2003b), Statistical 5-day tropical cyclone intensity forecasts derived from climatology and persistence, *Weather Forecast.*, *18*, 80–92, doi:10.1175/1520-0434(2003)018<0080:SDTCIF>2.0.CO;2.
- Knaff, J. A., T. A. Cram, A. B. Schumacher, J. P. Kossin, and M. DeMaria (2008), Objective identification of annular hurricanes, *Weather Forecast.*, *23*, 17–28, doi:10.1175/2007WAF2007031.1.
- Kossin, J. P., and M. D. Eastin (2001), Two distinct regimes in the kinematic and thermodynamic structure of the hurricane eye and eyewall, *J. Atmos. Sci.*, *58*, 1079–1090, doi:10.1175/1520-0469(2001)058<1079:TDRITK>2.0.CO;2.
- Maclay, K. S., M. DeMaria, and T. H. Vonder Haar (2008), Tropical cyclone inner-core kinetic energy evolution, *Mon. Weather Rev.*, *136*, 4882–4898, doi:10.1175/2008MWR2268.1.
- Merrill, R. T. (1984), A comparison of large and small tropical cyclones, *Mon. Weather Rev.*, *112*, 1408–1418, doi:10.1175/1520-0493(1984)112<1408:ACOLAS>2.0.CO;2.
- Montgomery, M. T., V. A. Vladimirov, and P. V. Denissenko (2002), An experimental study on hurricane mesovortices, *J. Fluid Mech.*, *471*, 1–32, doi:10.1017/S0022112002001647.
- Musgrave, K. D. (2011), Tropical cyclone inner core structure and intensity change, PhD dissertation, 103 pp., Dep. of Atmos. Sci., Colo. State Univ., Fort Collins.
- Ooyama, K. (1968), Numerical simulation of tropical cyclones with an axisymmetric model, in *Numerical Weather Prediction: Proceedings of the WMO/IUGG Symposium on Numerical Weather Prediction, Tokyo, November 26–December 4, 1968*, pp. 81–88, Meteorol. Soc. of Jpn., Tokyo.
- Ooyama, K. (1969), Numerical simulation of the life cycle of tropical cyclones, *J. Atmos. Sci.*, *26*, 3–40, doi:10.1175/1520-0469(1969)026<0003:NSOTLC>2.0.CO;2.
- Pendergrass, A. G., and H. E. Willoughby (2009), Diabatically induced secondary flows in tropical cyclones. Part I: Quasi-steady forcing, *Mon. Weather Rev.*, *137*, 805–821, doi:10.1175/2008MWR2657.1.
- Powell, M., and T. Reinhold (2007), Tropical cyclone destructive potential by integrated kinetic energy, *Bull. Am. Meteorol. Soc.*, *88*, 513–526, doi:10.1175/BAMS-88-4-513.
- Rosenberg, H. (1910), On the relation between brightness and spectral type in the Pleiades, *Astron. Nachr.*, *186*, 71–78, doi:10.1002/asna.19101860503.
- Rozoff, C. M., W. H. Schubert, and J. P. Kossin (2008), Some dynamical aspects of tropical cyclone concentric eyewalls, *Q. J. R. Meteorol. Soc.*, *134*, 583–593, doi:10.1002/qj.237.
- Schubert, W. H., and J. J. Hack (1982), Inertial stability and tropical cyclone development, *J. Atmos. Sci.*, *39*, 1687–1697, doi:10.1175/1520-0469(1982)039<1687:ISATCD>2.0.CO;2.
- Schubert, W. H., and B. D. McNoldy (2010), Application of the concepts of Rossby length and Rossby depth to tropical cyclone dynamics, *J. Adv. Model. Earth Syst.*, *2*, 7, doi:10.3894/JAMES.2010.2.7.
- Schubert, W. H., M. T. Montgomery, R. K. Taft, T. A. Guinn, S. R. Fulton, J. P. Kossin, and J. P. Edwards (1999), Polygonal eyewalls, asymmetric eye contraction, and potential vorticity mixing in hurricanes, *J. Atmos. Sci.*, *56*, 1197–1223, doi:10.1175/1520-0469(1999)056<1197:PEAECA>2.0.CO;2.
- Shapiro, L. J. (1983), The asymmetric boundary layer flow under a translating hurricane, *J. Atmos. Sci.*, *40*, 1984–1998, doi:10.1175/1520-0469(1983)040<1984:TABLFU>2.0.CO;2.
- Shapiro, L. J., and H. E. Willoughby (1982), The response of balanced hurricanes to local sources of heat and momentum, *J. Atmos. Sci.*, *39*, 378–394, doi:10.1175/1520-0469(1982)039<0378:TROBHT>2.0.CO;2.
- Smith, R. K., and M. T. Montgomery (2008), Balanced boundary layers in hurricane models, *Q. J. R. Meteorol. Soc.*, *134*, 1385–1395, doi:10.1002/qj.296.
- Smith, R. K., and S. Vogl (2008), A simple model of the hurricane boundary layer revisited, *Q. J. R. Meteorol. Soc.*, *134*, 337–351, doi:10.1002/qj.216.
- Smith, R. K., M. T. Montgomery, and S. V. Nguyen (2009), Tropical cyclone spin-up revisited, *Q. J. R. Meteorol. Soc.*, *135*, 1321–1335, doi:10.1002/qj.428.
- Terwey, W. D., and M. T. Montgomery (2008), Secondary eyewall formation in two idealized, full-physics modeled hurricanes, *J. Geophys. Res.*, *113*, D12112, doi:10.1029/2007JD008897.
- Vigh, J. L., and W. H. Schubert (2009), Rapid development of the tropical cyclone warm core, *J. Atmos. Sci.*, *66*, 3335–3350, doi:10.1175/2009JAS3092.1.
- Wang, Y. (2008), Structure and formation of an annular hurricane simulated in a fully compressible, nonhydrostatic model—TCM4, *J. Atmos. Sci.*, *65*, 1505–1527, doi:10.1175/2007JAS2528.1.
- Wang, Y. (2009), How do outer spiral rainbands affect tropical cyclone structure and intensity? *J. Atmos. Sci.*, *66*, 1250–1273, doi:10.1175/2008JAS2737.1.
- Weatherford, C., and W. M. Gray (1988a), Typhoon structure as revealed by aircraft reconnaissance. Part I: Data analysis and climatology, *Mon. Weather Rev.*, *116*, 1032–1043, doi:10.1175/1520-0493(1988)116<1032:TSARBA>2.0.CO;2.
- Weatherford, C., and W. M. Gray (1988b), Typhoon structure as revealed by aircraft reconnaissance. Part II: Structural variability, *Mon. Weather Rev.*, *116*, 1044–1056, doi:10.1175/1520-0493(1988)116<1044:TSARBA>2.0.CO;2.
- Willoughby, H. E., J. A. Clos, and M. G. Shoreibah (1982), Concentric eye walls, secondary wind maxima, and the evolution of the hurricane vortex, *J. Atmos. Sci.*, *39*, 395–411, doi:10.1175/1520-0469(1982)039<0395:CEWSWM>2.0.CO;2.
- Xu, J., and Y. Wang (2010a), Sensitivity of tropical cyclone inner core size and intensity to the radial distribution of surface entropy flux, *J. Atmos. Sci.*, *67*, 1831–1852, doi:10.1175/2010JAS3387.1.
- Xu, J., and Y. Wang (2010b), Sensitivity of the simulated tropical cyclone inner-core size to the initial vortex size, *Mon. Weather Rev.*, *138*, 4135–4157, doi:10.1175/2010MWR3335.1.
- Yamasaki, M. (1977), The role of surface friction in tropical cyclones, *J. Meteorol. Soc. Jpn.*, *55*, 559–571.
- Yanai, M., S. Esbensen, and J.-H. Chu (1973), Determination of bulk properties of tropical cloud clusters from large-scale heat and moisture budgets, *J. Atmos. Sci.*, *30*, 611–627, doi:10.1175/1520-0469(1973)030<0611:DOBPOT>2.0.CO;2.
- Zehr, R. M., and J. A. Knaff (2007), Atlantic major hurricanes, 1995–2005—Characteristics based on best-track, aircraft, and IR images, *J. Clim.*, *20*, 5865–5888, doi:10.1175/2007JCLI1652.1.

Corresponding author: K. D. Musgrave, Cooperative Institute for Research in the Atmosphere, Colorado State University, Fort Collins, CO 80523-1375, USA. (musgravek@cira.colostate.edu)